RSC Advances

PAPER

View Article Online
View Journal | View Issue

Cite this: *RSC Adv.*, 2025, **15**, 46674

Bacterial adhesion and erythrocyte integrity on polycaprolactone nanowire surfaces

Vignesh Sathyanarayanan, [ab] Liszt Y. C. Madruga, [b] Bruno Leandro Pereira, [c] Paulo Soares [c] and Ketul C. Popat [*ab]

Blood-contacting devices (BCDs), such as blood collection bags, blood tubes, artificial heart valves, vascular grafts and catheters, are subject to complications such as thrombosis, restenosis, hemolysis *etc.* These complications result in poor hemocompatibility and bacterial infections on the surfaces of BCDs that ultimately affect the patient's health. Natural and synthetic biocompatible polymers are used as potential solutions for these issues due to their superior biodegradability. Recent advancements in nanoscale fabrication and modification of these surfaces have shown improved results with platelets, leukocytes and other whole blood components. However, disruptions in erythrocyte's cell structure, caused by the foreign body materials, can compromise their oxygen-carrying capacity. This can further affect the overall tissue oxygenation and potentially lead to myocardial ischemic conditions. Therefore, it is vital to understand the effect of BCD's surface properties on erythrocyte integrity and viability. Additionally, bacterial adhesion on these BCDs surfaces can cause severe infections like bacteremia, that can further escalate into sepsis. Biofilms and bacterial colonies can act as pro-thrombotic surfaces themselves, which increases the risk of device-associated thrombosis. Hence, improving the antibacterial properties of the BCDs surfaces is also essential to prevent bacterial growth and biofilm formation on its surfaces. In this study, PCL nanostructured surface: nanowires were fabricated and modified with organic compounds: Tanfloc (TN) and Carboxymethyl Kappa-Carrageenan (CMKC) to investigate their antibacterial properties and their effect on erythrocyte's cell integrity. Results indicate that the modified PCL nanowires retain the erythrocyte integrity better and exhibit enhanced antibacterial properties.

Received 17th July 2025
Accepted 17th November 2025

DOI: 10.1039/d5ra05152e

rsc.li/rsc-advances

1. Introduction

Blood-contacting devices (BCDs) are critical components in modern medicine.[1] Some of the examples of BCDs are catheters, blood tubes, blood collection bags, heart valves, vascular grafts *etc.*[2] These devices are commonly used in procedures such as vascular interventions,[3] hemodialysis[4] and organ support systems.[5] Failure of BCDs lead to catastrophic consequences as well as imposing severe financial burdens on the patients. Thus, enhancing the success rate of BCDs applications can potentially lower the cost associated with cardiovascular disease treatment and contribute to improved patient outcomes. The main cause of failure of BCDs is poor hemocompatibility, which leads to a cascade of adverse biological responses. In addition to poor hemocompatibility, contaminated BCDs can become breeding grounds for pathogens which can lead to concerning risks of bloodstream infections (BSIs). Therefore, the design of BCDs is heavily influenced by the ongoing challenge of achieving antibacterial properties and sufficient hemocompatibility while preserving the structural and functional integrity of erythrocytes (red blood cells).[2]

One of the primary issues associated with BCDs is their surface properties.[6] The physical and chemical characteristics of the material surfaces can significantly alter the behavior of erythrocytes and other blood components upon contact.[7] Such alterations can lead to the erythrocyte dysfunction, potentially resulting in the circulation of deoxygenated blood and causing life-threatening conditions within the host.[8] For instance, currently used polymeric materials for these BCDs include polyvinyl chloride (PVC), polyurethanes (PUs), polyethylene terephthalate (PET) and fluorinated polymers.[9] However, studies reveal that they can potentially lead to complications due to poor hemocompatibility, thrombus formation and altered erythrocyte's morphology and functionality.[10,11] The primary factors that affect the erythrocytes interactions with the surfaces include surface wettability, surface charge and the surface topography of the polymers used.[12] Furthermore, pathogenic bacteria such as *Staphylococcus aureus* and *Pseudomonas aeruginosa* exploit favorable conditions for growth and biofilm formation, leading to high rates of BSIs.[13,14] Therefore, the

[a]*Department of Mechanical Engineering, Colorado State University, Fort Collins, CO 80523, USA. E-mail: kpopat@gmu.edu*

[b]*Department of Bioengineering, George Mason University, Fairfax, VA 22030, USA*

[c]*Department of Mechanical Engineering, Pontificia Universidade Católica Do Paraná, Curitiba 80215-901, PR, Brazil*

selection and fabrication of BCDs should prioritize polymeric materials with hemocompatibility and antibacterial properties, as their physical and chemical surface characteristics are crucial in preventing erythrocyte dysfunction and BSIs.

Polycaprolactone (PCL), a synthetic polymer, has been shown as a potential biomaterial for BCDs due to its unique properties that enhance biocompatibility and functionality. The ability of PCL to be fabricated into different complex geometries, using techniques like electrospinning and 3D printing, enables a vast range of applications for it.[15,16] This property allows it to be customized into a variety of medical devices, ranging from utilization for BCDs to implants that fit specific patient anatomies.[17] The hydrophobic nature of PCL often limits cell adhesion and proliferation; however, the introduction of nanostructures modifies the surface properties to improve wettability and promote cellular interactions.[18] Nanostructured surfaces can provide topographical cues that influence cell behavior. Moreover, nanostructured PCL surfaces can also be engineered to significantly decrease the contact area between bacteria and the surface. For instance, studies have demonstrated that nanopillared PCL surfaces effectively inhibited bacterial adhesion and biofilm formation, primarily due to their reduced contact area and mechanical rupture of bacterial membranes.[19] The sharp edges and high aspect ratios of nanostructures can induce physical damage to bacterial cells on contact, leading to cell lysis or impaired function.[20,21] Previous studies have demonstrated that the introduction of nanoscale features, such as nanowires, increased the surface area available for cell attachment, thereby promoting stronger cell–substrate interactions.[22,23] The whole blood clotting kinetics, platelet adhesion and activation were also investigated on nanostructured surfaces such as nanofibers and nanowires.[24,25] However, not many studies are done specifically about erythrocytes interaction with nanostructured PCL surfaces.

Furthermore, the addition of organic compounds on the biomaterials plays a crucial role in enriching its hemocompatibility and antibacterial properties, which are necessary for successful functioning of the BCDs with the host body. Tanfloc (TN) coatings, derived from condensed tannins, have gained attention in the field of biomaterials for its multifaceted benefits, particularly in enhancing biocompatibility, antibacterial properties and promoting osteogenesis. The unique chemical structure of TN, which includes catechol and pyrogallol groups, contributes to its superior antimicrobial activity compared to other natural polycations like chitosan.[26,27] Studies have demonstrated that TN/heparin polyelectrolyte multilayers significantly enhance blood compatibility by reducing fibrinogen adsorption and platelet adhesion, which are critical factors in preventing thrombosis on implant surfaces.[27,28] This becomes an important characteristic for BCDs, where maintaining blood flow and minimizing clot formation are essential for the longevity of the device and patient's health. Additionally, TN's inherent antibacterial properties contribute to its effectiveness in preventing biomaterial associated infections. The mechanism of action includes enzyme inactivation and chelation of trace metal ions, which disrupts bacterial growth and biofilm formation.[26,29] Similarly, Carboxymethyl Kappa-Carrageenan (CMKC) derived from kappa-carrageenan, a natural polysaccharide extracted from red algae, has shown to be advantageous due to its biocompatibility, biodegradability and non-toxicity.[30] Studies have shown that CMKC exhibits favorable interactions with human cells, enhancing cell adhesion and proliferation.[31] CMKC has also shown to significantly reduce bacterial colonization, which is an important factor in selection of biomaterial for BCDs. But very few studies have been done, incorporating these organic compounds with nanostructured polymeric surfaces, to understand its effects on the erythrocytes cell integrity and antibacterial properties.

In this study, Nanowires (NW) were fabricated from PCL control surfaces using nano-templating method. Additionally, the NW surfaces were modified with organic compounds – TN and CMKC, to study their effects on the erythrocyte cell integrity and antibacterial properties. The surface morphology and topography of different surfaces were characterized using Scanning Electron Microscopy (SEM). The surface wettability was evaluated by measuring contact angles *via* goniometry. X-ray photoelectron spectroscopy (XPS) and X-ray diffraction (XRD) crystallography were used to evaluate the surface chemistry and surface crystallinity. To understand the mechanical properties of all the surfaces, indentation hardness and elastic modulus were analyzed using the nanoindentation technique. Erythrocyte cytotoxicity was evaluated using commercially available LDH assay kit. Erythrocyte cell adhesion was examined using Rhodamine-Phalloidin (F-actin) stain under fluorescence microscopy and erythrocyte cell morphology was characterized using SEM. Finally, the antibacterial properties of the surfaces were investigated with Gram-positive *Staphylococcus aureus* and Gram-negative *Pseudomonas aeruginosa* bacteria using SEM and live/dead bacteria staining. The results indicated that the NW surfaces modified with organic compounds exhibited enhanced antibacterial properties and retained the erythrocyte cell integrity significantly, while being non-cytotoxic to the erythrocytes.

2. Experimental details

2.1. Fabrication of PCL control (PCL) surfaces

PCL control surfaces (PCL) were fabricated using a Prusa i3 3D printer with a nozzle diameter of 1.75 mm. Facilan™ PCL 100 Filament, with a diameter of 1.75 mm and molecular mass of 50 kDa, was used to 3D print PCL discs of 10 mm diameter and 2 mm thickness on a flatbed. The nozzle and bed temperature of the printer were set to 180 °C and 45 °C, respectively. The printed control discs were collected in a well plate and stored in a desiccator overnight to remove moisture from the control surfaces.

2.2. Fabrication of PCL nanowire (NW) surfaces

Commercially available 20 nm diameter nanoporous aluminium oxide membranes (ANOPORE™, Whatman) were used to fabricate PCL Nanowire (NW) surfaces using the solvent-free nano-templating process. The PCL control surfaces were placed on the nanoporous membrane surface inside a custom-

made 3D printed template and were covered with glass slides on the top and bottom. The polymer control surfaces, placed on the nanoporous alumina membrane, were allowed to gravimetrically extrude through the membrane for 15 minutes at 74 °C in an oven. The extruded NWs were then released by dissolving the aluminium oxide membranes in 1 M NaOH for 75 minutes.[32] Once dried, the NW surfaces were washed thrice with DI water and then stored in a desiccator to remove moisture from the surfaces.

2.3. Modification of PCL nanostructured surfaces

2.3.1 Tanfloc purification. Tanac SA (Montenegro-RS, Brazil) has generously donated Tanfloc (TN), an amino-functionalized polyphenolic tannin derivative with a molecular weight of approximately 600 kDa,[33] which was then purified for this study. The Commercial TN product is produced by polymerizing tannin with the addition of formaldehyde, ammonium chloride, and hydrochloric acid.[34] Dialysis can remove the excess chloride ions in the TN structure transferred from the ammonium chloride used in TN synthesis. The hydrolyzable tannins and other low molecular weight substances in the commercial TN can also be removed through dialysis. A solution of TN in sodium acetate buffer (pH 5.0 and 0.2 mol L^{-1}) was produced at a concentration of 10 g L^{-1} and stirred overnight on a magnetic stir plate to ensure complete dissolution. The TN solution was then dialyzed using a Snakeskin Dialysis Tubing (10 kDa MWCO) in DI water for three consecutive days. The dialysate (DI water) was replaced bi-daily to maintain its purity during dialysis. After the 72-hours dialysis, the solution was filtered using a Whatman filter paper (110 mm) to eliminate residual contaminants. The filtered TN solution was frozen at −80 °C and lyophilized for five days to yield a dry, purified TN.[33,35]

2.3.2 CMKC synthesis. Kappa-carrageenan (KC) containing small amounts of iota-carrageenan and monochloroacetic acid (MCA) were purchased from Sigma-Aldrich (USA). The Carboxymethyl-Kappa-Carrageenan (CMKC) was synthesized for this study. The carboxymethylation of KC was done following Williamson's ether synthesis method. The system used for the carboxymethylation process consists of a 250 mL three-necked glass flask combined with a reflux condenser, thermometer, and a mechanical stirrer placed in a water bath. For the reactions, 2 g of KC was suspended in 40 mL of an aqueous solution containing 80% (w/v) of 2-propanol in the 3-necked glass flask coupled with a reflux condenser. 4 mL of a 20% NaOH aqueous solution was added dropwise over 15 minutes. The mixture was stirred rapidly at 40 °C for 1 hour. Monochloroacetic acid solution (MCA) was dissolved in 4 mL of 20% NaOH aqueous solution and stirred at ambient temperature for 30 minutes to achieve alkaline activation. The activated MCA solution was then added dropwise using a syringe to the KC solution for a duration of 20 minutes while maintaining a temperature of 55 °C for 4 hours of stirring. The reaction was carried out with the degree of substitution (DS) being 1.1 for the molar ratios of MCA to KC monomer of 3.5 : 1. Previous studies have reported the confirmation of DS of CMKC using ^{1}H NMR spectroscopy. Following the reaction, the product was isolated using vacuum filtration and washed thrice with 80% 2-propanol aqueous solution and pure 2-propanol. Later, the product was dried in an oven at 50 °C for an entire night. The resultant powder was dissolved in 300 mL of DI water overnight and underwent dialysis against water using a membrane with a maximum molecular weight cut-off (MWCO) 7000 Da (pore 22 × 35 mm) until the conductivity went below 20 μS cm^{-1}. Ultimately, the product was lyophilized in a ModulyoD lyophilizer (ThermoSavant), resulting in CMKC (M_w = 4.3 ×10^5 $gmol^{-1}$) with a DS of 1.1, as mentioned above. The reaction conditions were uniform for both products.[30,36]

2.3.3 Layer-by-layer deposition. The experimental procedure used to prepare the Layer-by-Layer (LbL) deposition was adapted from the methods that had been previously reported.[33,35] In this procedure, NW surfaces were modified by treating them with TN and CMKC solutions to obtain modified nanostructured surfaces. The following notations will be used throughout the manuscript – NW modified with TN: NW_{TN}; and NW modified with TN followed by CMKC: $NW_{TN+CMKC}$ groups. TN (polycation) and CMKC (polyanion) solutions were prepared in an acetic acid-acetate buffer (0.2 M sodium acetate and acetic acid at pH 5.0) at a concentration of 5 mg mL^{-1} and 1 mg mL^{-1} respectively. The solutions were stirred overnight. After that, the solutions were filtered using 0.22 μm polyvinylidene fluoride (PVDF) syringe filters from Fisher Scientific (Waltham, MA, USA). An aqueous acetic acid solution (pH 4.0) was used as a rinse solution. Prior to surface modification with polyelectrolytes, the NW surfaces were treated with oxygen plasma at 200 V in 10 cm^3 min^{-1} of oxygen gas for 5 minutes. The surfaces were placed in 24-well plates and were modified *via* oxidation using oxygen plasma to facilitate the deposition of the polyelectrolytes. The rinse and deposition steps were all conducted on an orbital shaker (100 rpm). The oxidized surfaces were rinsed with the rinse solution for 4 minutes before the LbL deposition. The rinse solution was aspirated, and LbL deposition was carried out on the oxidized surfaces by adding the TN solution (polycation). After 5 minutes, the TN solution was aspirated, and the surface was rinsed again for 4 minutes. Subsequently, the rinse solution was aspirated, and the surfaces were washed with DI water for 30 seconds to obtain NW_{TN} surfaces. For $NW_{TN+CMKC}$, an additional layer of CMKC solution was deposited on the surfaces. The CMKC (polyanion) solution was added to the oxidized surfaces containing one layer of polycation (TN) for 5 minutes. Then, the CMKC solution was aspirated, and the surfaces were rinsed for 4 minutes. Finally, the rinse solution was aspirated, and the surfaces were washed with DI water for 30 seconds. Following this LbL deposition, all the modified surfaces were stored in a desiccator until further use.

2.4. Surface characterization

2.4.1 Surface morphology. The surface topography of different nanostructured surfaces was examined using scanning electron microscopy (SEM, JEOL JSM-6500F). Prior to imaging, a 10 nm coating of gold was applied to the surfaces for improved conductivity. The parameters for the SEM were optimized and chosen as follows: accelerating voltage of 5 kV, working distance

range: 7–12 mm, and vacuum pressure below 3×10^{-4} Pa. The working distance, brightness and contrast were adjusted for each surface to ensure similar quality of images. SEM images were captured at varying magnifications ranging from 500× to 7500× magnification.

2.4.2 Surface wettability. Goniometer was used to determine the surface wettability of different surfaces by measuring contact angle measurements using a sessile drop measuring technique with the Ramè-Hart goniometer (Ramé-Hart Instrument Co., Succasunna, NJ, USA). The apparent contact angle was measured 3 s after a 10 μl drop of DI water was placed on the surface using the DROPimage software.

2.4.3 Surface chemistry. XPS (PHI Physical Electronics PE-5800 X-ray Photoelectron Spectrometer with an Al Kα X-ray source) was used to characterize the surface chemistry of different surfaces. XPS survey scans were collected for all the surfaces to understand the overall atomic composition. Survey spectra for all the surfaces were collected from 0 eV to 1100 eV. Peak-fit analysis was conducted using CasaXPS (Version 2.3.25PR1.0). From the survey spectra, elemental analysis was also conducted for each surface using CasaXPS (Version 2.3.25PR1.0) and the composition (atomic weight percentage, % at) of each element was recorded.

2.4.4 Surface crystallinity. XRD (XRD-7000 Shimadzu) was used to analyze the crystalline structure of the surfaces, while using CuKα radiation at 40 kV and 30 mA. When performing XRD, a thin film (TF-XRD) geometry was utilized for the surfaces with a fixed incidence angle of 5°. Diffractograms were acquired with continuous scans from 20° to 80° at scanning speed of $1° \text{ min}^{-1}$. Peaks were indexed using Match! software with the PDF-2 Database.

2.4.5 Mechanical properties. Nanoindentation technique was used to characterize the mechanical properties of the surfaces, such as surface hardness (H) and elastic modulus (E). A Zwick-Roell/Asmec nano-indenter was used to examine these mechanical properties. It was programmed by an array (5 × 5), with 50 μm between each indentation and 0.1 N of maximum applied force on the surface by a calibrated Berkovich tip. To enhance measurement accuracy, the quasi-continuous stiffness measurement (QCSM) technique was implemented. This method allows for high accuracy measurements due to a progressively increasing force (from 0–100 mN for this study) combined with a dwell time at each force point.

2.5. Erythrocyte interaction with different surfaces

2.5.1 Isolation of erythrocytes from whole human blood. Human blood samples were drawn from healthy volunteers at Colorado State University, with informed consent secured prior to collection, in accordance with protocols approved by the CSU Institutional Review Board and adhering to NIH ethical guidelines. The whole blood was collected into EDTA vials and centrifuged (500 g, 10 min, 4 °C) to separate plasma, buffy coat and erythrocytes. Then the plasma and buffy coat were aspirated, and the erythrocyte layer was resuspended in PBS (pH 7.4) to a final concentration of 10^7 cells per mL. Surfaces were washed with DI waster and PBS and were sterilized with 70% ethanol (30 minutes) and UV light (30 minutes). Sterilized surfaces were then incubated with 500 μL erythrocyte suspension for 1.5 and 6 hours at 37 °C in 24-well plates.

2.5.2 Cytotoxicity of different surfaces. To assess the cytotoxicity induced by different surfaces, a lactate dehydrogenase (LDH) based indicator assay was utilized (Cayman's LDH Cytotoxicity Assay Kit). After 1.5 hours of incubation of different surfaces with erythrocytes, 100 μL supernatants of the cell media were transferred from each surface to a new sterile 96-well plate. A 100 μL of LDH reaction solution was added to each well containing the cell supernatants that were previously added to the 96-well plate. The well plate was incubated at 37 °C with 5% CO_2 for 30 minutes. The plate reader measured the absorbance of the resultant solution at a wavelength of 490 nm. A negative control (highest LDH release) was established by lysing erythrocytes with 10% Triton-X100. The positive control (Sp, indicating spontaneous release) was prepared using erythrocyte suspension without any surface exposure. The assay protocol provided by the manufacturer was followed to determine the cytotoxicity induced by the surfaces against erythrocytes and thus the cytotoxicity was calculated.

2.5.3 Erythrocyte adhesion on different surfaces. Erythrocyte adhesion on different surfaces was characterized using fluorescence microscopy. Rhodamine-Phalloidin (F-actin stain) was used to stain the adhered erythrocyte cells on the surfaces. The stock solution was prepared by resuspending the vial in 500 μL of 100% methanol (14 μM). The working solution was prepared by resuspending 11.25 μL of the stock solution in 2.25 mL PBS (final concentration 70 nM). The erythrocyte suspension from the incubated surfaces was aspirated to remove floating cells, and the surfaces were rinsed twice with PBS to remove the rest of the non-adherent cells. Then, the fixative (3.7% formaldehyde in PBS) was added to the surfaces with adhered cells and incubated for 15 minutes at ambient room temperature. Subsequently, the fixative solution was aspirated and rinsed with PBS thrice after the incubation. Then, the permeative (1% Triton X-100 in DI water) was added to all surfaces and incubated at room temperature for three minutes. Later, the permeative solution was aspirated, and the surfaces were rinsed thrice with PBS to ensure complete removal of any residual solution. Then, the surfaces were exposed to the staining solution, prepared at a concentration of 1 : 200 (50 μL rhodamine + 10 mL PBS), and incubated at room temperature for 25 minutes. Finally, the staining solution was aspirated, and the surfaces were rinsed with PBS. The surfaces were then hydrated with PBS, just enough to be immersed in. The well-plates with the surfaces were immediately covered with aluminum foil to avoid any contact with ambient lights. The surfaces were imaged using a fluorescent microscope (Zeiss). Each surface was imaged at three different locations at a magnification of 20×. The images were processed with ImageJ to adjust their brightness and contrast. The entire procedure, from staining to imaging, was performed in darkness.

2.5.4 Erythrocyte morphology on different surfaces. The morphology of adhered erythrocytes on different surfaces was characterized using SEM. After the erythrocytes incubation, the media was aspirated, and the surfaces were washed once with

PBS for 5 minutes. Then, the surfaces were incubated with a primary fixative solution comprising 3% glutaraldehyde (Sigma-Aldrich, St. Louis, MO, USA), 0.1 M sucrose (Sigma-Aldrich, St. Louis, MO, USA) and 0.1 M sodium cacodylate (Electron Microscopy Sciences, Hatfield, PA, USA) in DI water for 45 minutes at ambient temperature. Following this, the fixative solution was removed, and the surfaces were incubated with a buffer solution containing the fixative, except glutaraldehyde, for 10 minutes. At last, the surfaces were dehydrated with 35%, 50%, 70% and 100% ethanol solution, each for a 10-minutes incubation period. Prior to SEM imaging, the surfaces were stored in a desiccator to ensure dryness. Before placing the surfaces in the SEM apparatus, a 10 nm gold coating was applied using a Denton Vacuum Desk II Gold Sputter Coater to enhance the surface conductivity of the polymer surfaces for imaging purposes.

2.6. Evaluation of antibacterial properties

2.6.1 Bacteria culture. Gram-positive *Staphylococcus aureus* (*S. aureus*, ATCC6538) and Gram-negative *Pseudomonas aeruginosa* (*P. aeruginosa*, ATCC10145) bacterial strains were utilized to access the antibacterial properties of different surfaces. Both bacterial strains were cultured in tryptic soy broth (TSB, Sigma-Aldrich, St. Louis, MO, USA) at 37 °C for 24 hours until a concentration of 10^9 Colony Forming Units (CFU) mL^{-1} was attained. The CFU mL^{-1} was quantified by analyzing the absorbance values of the bacterial solution using a plate reader at a wavelength of 562 nm. A diluted bacterial culture of 10^6 CFU mL^{-1} was used to examine bacterial adhesion and morphology on different surfaces. The surfaces were placed in a 24-well plate and sterilized with 70% ethanol for 30 minutes. Then, they were air dried, further sterilized under UV light for 30 minutes, and subsequently rinsed twice with PBS for 5 minutes each. After sterilization, the surfaces were incubated with the 10^6 CFU mL^{-1} bacterial solution for 6 hours and 24 hours at 37 °C in an incubator. Following incubation, the surfaces were washed twice with PBS for 5 minutes to remove any non-adhered bacteria prior to further characterization.

2.6.2 Bacteria adhesion on different surfaces. A fluorescent microscope was used to determine the amount of live or dead bacteria adhering to different surfaces. Post incubation of the surfaces with the bacteria media for 6 hours and 24 hours, the media was aspirated, and surfaces were rinsed with PBS for 5 minutes each. Then, the surfaces were incubated at room temperature for 15 minutes in a staining solution comprising a 1 : 1 ratio of propidium iodide (dead bacteria stain) and Syto 9 (live bacteria stain) at a concentration of 3 μL mL^{-1} in PBS (ThermoFisher Scientific, Waltham, MA, USA). The stain solution was then removed, and the surfaces were rinsed again with PBS and incubated with 3.7% formaldehyde (Fisher Chemical, Fair Lawn, NJ, USA) for 15 minutes at ambient room temperature to fix the cells adhering to the surfaces. Subsequently, the formaldehyde was aspirated, and the surfaces were washed with PBS twice for 5 minutes each and stored in PBS. Ultimately, the surfaces were imaged using a fluorescence microscope (Zeiss). ImageJ was used to determine the percentage of the area fraction covered by the live or dead bacteria on the surfaces. The entire procedure, from staining to imaging, was performed in darkness.

2.6.3 Bacteria morphology on different surfaces. The morphology of adhered bacteria on different surfaces was characterized using SEM. Prior to SEM imaging, the bacteria adhered to the surfaces were fixed using a standard fixing procedure. The procedure for this study follows the same steps as done for erythrocyte morphology, as mentioned earlier in Section 2.5.4.

2.7. Statistical analysis

Surface characterizations were done using at least 3 different samples for each surface, at 3 different locations on the surface ($n_{min} = 9$). For cytotoxicity, a minimum of four samples ($n_{min} = 4$) of each surface were utilized and the experiments were repeated at least twice ($n_{min} = 8$). In the erythrocyte adhesion, morphology and anti-bacterial activity studies, a minimum of three samples ($n_{min} = 3$) of each surface were utilized and all experiments were repeated at least thrice ($n_{min} = 9$). Statistical one-way analysis of variance (ANOVA) and post-hoc analysis (*t*-tests) were conducted for the experiment data using OriginPro 2024 software at a 5% significance level ($p \leq 0.05$).

3. Results and discussion

3.1. Surface morphology

The morphological features on the surfaces play a crucial role in affecting the cell and bacteria adhesion on surfaces.[37,38] SEM images of PCL do not show any unique topography (Fig. 1). As expected, the PCL surfaces have considerable roughness and irregularities due to its processing and are not naturally smooth. The NW surfaces are formed by gravimetrically extruding PCL control surfaces *via* nanoporous anodic aluminum oxide membranes at a temperature slightly greater than the glass transition temperature of PCL.[39] The SEM images

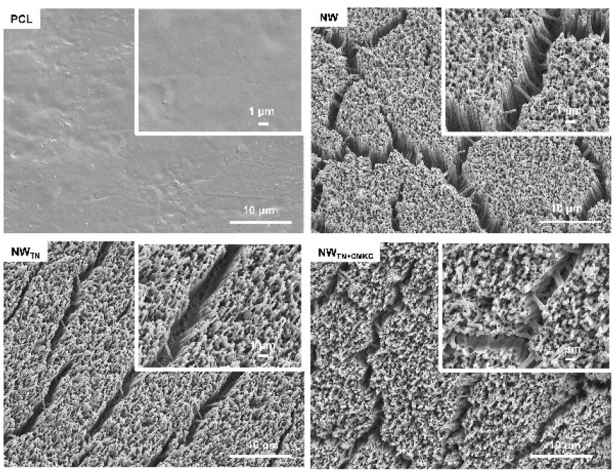

Fig. 1 Representative SEM images of different surfaces at low (2500×) and high magnification (insert, 7500×). Scale bars of low and high magnification images indicate 10 μm and 1 μm, respectively.

of NW surfaces show an evenly distributed uniform architecture of extrusions, perpendicular to their surface (Fig. 1). These SEM images of NW indicate that their morphologies have a unique texture topography contrasting to the non-textured PCL surface. Using ImageJ, the height and the diameter of the NWs were computed to be 1.57 ± 0.17 μm and 341.43 ± 31.96 nm respectively. This study conformed with the previous literature that have shown similar NW surfaces produced, which enhances cellular functionality.[40,41] The increase in the diameter of the NWs compared to the nominal pore size of the alumina membrane can be attributed to the static surface change and surface tension effects following the expansion of the polymerized NWs after the lateral dissolution of alumina membranes in NaOH.[25,39] After the LbL deposition of TN and CMKC on different surfaces, the SEM images indicate no visible changes as compared to unmodified surfaces. Thereby, the evidence suggests that the NW surfaces maintain a stable nanoarchitecture throughout the LbL deposition process.

3.2. Surface wettability

Surface wettability is an important surface characteristic of a biomaterial that has shown to influence interactions of blood components with surfaces.[42,43] The contact angle is measured between the surface and tangent line at the point of contact of the liquid droplet with the surface. Contact angle (θ) depends on various surface properties such as surface area, topography, energy, polarity due to chemistry *etc.* This angle provides insight about the liquid and the solid surface, which are influenced by the above-mentioned surface properties. Generally, the wettability of surfaces can be categorized into different types based on its contact angle: hydrophilic if $\theta < 90°$, indicating that the liquid tends to spread across the surface, hydrophobic if $\theta > 90°$, indicating that the liquid droplet maintains a more spherical shape and does not spread out much on the surface.[44,45] Furthermore, superhydrophilic surfaces can have $\theta < 5°$, allowing the water droplet to spread almost completely across the surface.[46]

Results indicate that the PCL surface was almost hydrophobic as expected, with contact angle value 80.2° ± 10.6° (Fig. 2). This hydrophobic nature of PCL is attributed to its densely packed semi-crystalline structure, which limits water penetration and interaction with biological fluids.[47,48] All the other treated surfaces exhibited a significantly reduced contact angle with respect to the PCL control. The NW, NW_{TN} and $NW_{TN+CMKC}$ surfaces were all hydrophilic with values 21.9° ± 7.0°, 12.5° ± 2.9° and 22.1° ± 5.5° respectively (Fig. 2). This is because, NWs have increased surface area to volume ratio which enhances their hydrophilic characteristics. Also, their compact and elongated nanostructures, tend to trap water within them, further enhancing the material's apparent hydrophilicity.[49,50] There was no significant difference in terms of wettability between the NW and modified NW surfaces.[51,52]

3.3. Surface chemistry

The PCL control surface underwent several surface modifications to improve its hemocompatibility and enhance antibacterial properties. Hence, it is vital to understand the surface chemistry of different surfaces before and after modifications. Moreover, evaluating the surface chemistry is necessary to understand if LBL deposition of TN and CMKC was successful.

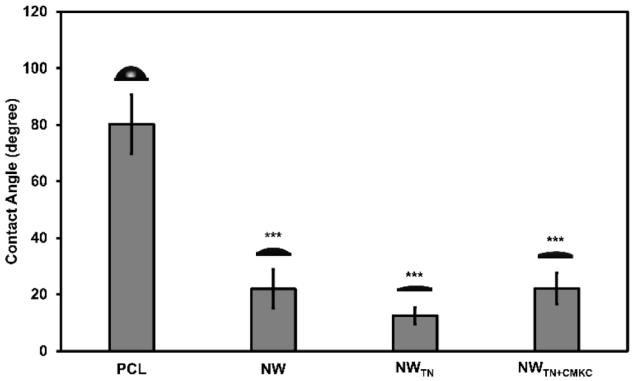

Fig. 2 Static water contact angle of different surfaces. Images of water droplet on the surfaces are also shown in the plot. Statistical significances (p-value) were represented as *** for $p < 0.001$ when compared to PCL control.

The XPS survey scan depicts comparison between PCL control and all other surfaces at different bonding energies ranging from 100 eV to 700 eV (Fig. 3). From the survey scan of PCL control, the presence of C 1s peak (284.6 eV) and O 1s peak (530 eV) was detected, which is typical of the PCL XPS spectrum reported in previous literature.[53] NW were also exhibiting the same peaks of C 1s and O 1s, indicating that there was no change in the surface chemistry of the nanostructured PCL surfaces in comparison to the PCL control. However, after the LbL deposition of TN, both the modified surfaces (NW_{TN} and $NW_{TN+CMKC}$) exhibited a new peak at binding energy 400 eV (N 1s) that corresponds to the presence of nitrogen on the surfaces (Fig. 3). This N 1s presence was due to the successful modification of surfaces with TN. The N 1s peak can be attributed to

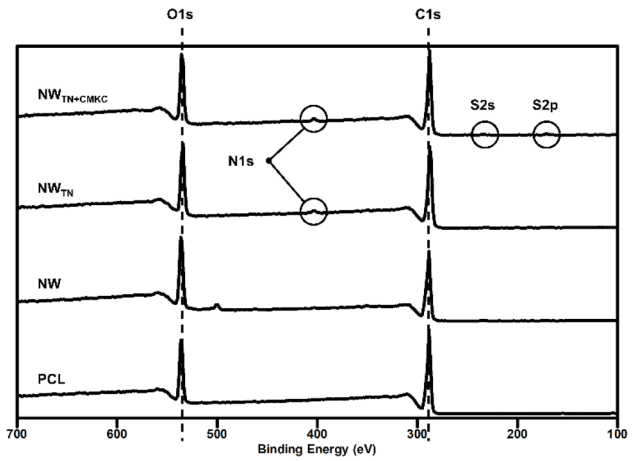

Fig. 3 XPS survey scan spectra of different surfaces. Peaks corresponding to C 1s and O 1s are characteristic of PCL, while the appearance of N 1s and S 2p peaks after modification confirm the presence of TN and CMKC functional groups on NW surfaces. The relative changes in elemental composition demonstrate successful LbL surface modification.

Table 1 Elemental analysis (% atomic) of different surfaces from XPS survey spectra

	% C 1s	% O 1s	% N 1s	% S 2p
PCL	76.53	23.47	0.00	0.00
NW	69.79	30.21	0.00	0.00
NW_{TN}	73.35	25.06	1.58	0.00
$NW_{TN+CMKC}$	71.58	26.24	1.55	0.63

the characteristic composition of TN because of the presence of amine groups in it.[33] However, $NW_{TN+CMKC}$ exhibited additionally a small peak at binding energy 168 eV which corresponds to the traces of sulphur (S 2p).[54] Presence of S 2p peak is attributed to the sulphate group which belongs to CMKC.[55] This is due to the sulfation process that kappa carrageenan undergoes during its extraction and purification from algae.[56] The sulphur atoms in kappa carrageenan are primarily associated with sulphate ($-SO_4$) moieties, which are integral to its biological and physicochemical properties.[57] Therefore, the XPS survey scan confirms the successful LbL deposition of TN and CMKC.

From the XPS survey scans, the elemental composition (atomic weight percentage, % atomic) of the surfaces was calculated as shown in Table 1. PCL and NW surfaces showed no traces of nitrogen or sulphur as expected. On the other hand, both the modified surfaces (NW_{TN} and $NW_{TN+CMKC}$) showed the presence of nitrogen. Also, the $NW_{TN+CMKC}$ surfaces displayed minute traces of sulfur as expected.

3.4. Surface crystallinity

To characterize surface crystallinity and phase composition of the materials, XRD is a pivotal technique. The characterization of PCL control and nanostructures is important for understanding the physical properties which directly influence its functionality as a biomaterial. In addition to crystallinity, XRD also serves as a fundamental tool to estimate the presence of any secondary phases or impurities within PCL nanostructured surfaces. The XRD patterns of different surfaces are presented in Fig. 4. PCL is a semi-crystalline polymer characterized by distinct peaks in its XRD patterns. Results indicate that PCL control shows a significant crystalline peak approximately at 21.5° and a relatively low intensity peak at about 23.5°,[58–60] which are attributed to the (110) and (200) lattice planes of its orthorhombic crystal form, respectively.[61] These values align with the Joint Committee on Powder Diffraction Standards (JCPDS #50-2459) reference for PCL, which confirms the orthorhombic crystalline structure of the polymer.[62] These sharp peaks indicate a high degree of crystallinity, which is an important property influencing the mechanical and thermal behavior of the polymer.[63] The XRD patterns of NW and modified NW groups also remain consistent with the patterns of PCL control.[66,67]

3.5. Mechanical properties

Understanding the mechanical properties such as material hardness, elastic modulus, stiffness and flexibility of materials is essential to determine the influence of biological interactions

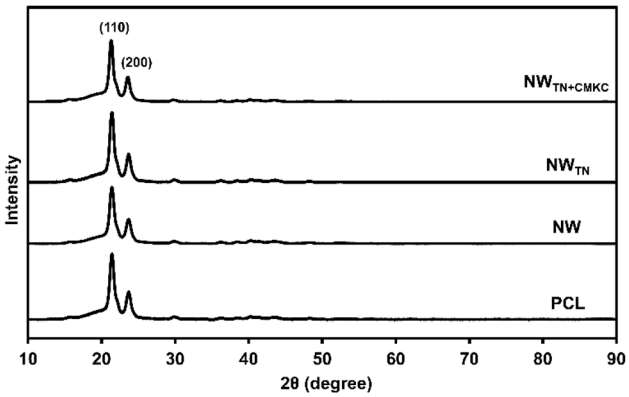

Fig. 4 XRD spectra of different surfaces. Characteristic diffraction peaks of PCL at $2\theta = 21.5°$ and 23.5° are evident in all samples, corresponding to the orthorhombic crystalline phase of PCL. The NW fabrication did not alter the intrinsic crystallinity of PCL. After TN and CMKC deposition, no new crystalline peaks ware observed, consistent with the amorphous nature of polyelectrolyte coatings. This confirms that the surface modifications did not disrupt the bulk crystalline structure of PCL NWs.

and material performance in biomedical applications.[64] Studies have shown that mechanical signaling from the surrounding microenvironment influences the interaction of cells with surfaces.[65,66] Hence, to understand these mechanical properties, indentation hardness and elastic modulus of all the surfaces were determined using the nanoindentation technique.

Fig. 5A shows the indentation hardness *vs.* displacement plots of different surfaces. Results show very similar range of hardness values for NW (0.03 ± 0.02 GPa) and modified NW surfaces (NW_{TN} = 0.1 ± 0.01 GPa, $NW_{TN+CMKC}$ = 0.04 ± 0.01 GPa) when compared with PCL control (0.08 ± 0.01 GPa). The linear structure of NW surfaces does not effectively distribute loads, resulting in fewer points of resistance during indentation, thereby contributing to its lower initial hardness. As the displacement increases, the NW surfaces show longer plateau regions before failure (displacements ranging from 11 to 14 μm) at lower hardness values (0.05 ± 0.02 GPa). This indicates a deeper penetration of the indenter into the material, suggesting its enhanced deformation tolerance prior to local failure under indentation. Elastic modulus curves (Fig. 5B) also show a similar qualitative trend to the hardness curves for the NW surfaces. No practically meaningful separation in near-surface

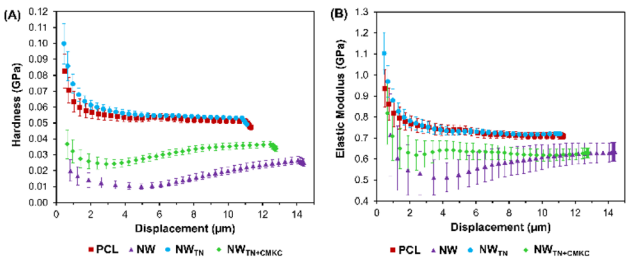

Fig. 5 (A) Indentation hardness (GPa) *vs.* displacement (μm) and (B) elastic modulus (GPa) *vs.* displacement (μm) for different surfaces.

elastic modulus *vs.* displacement was resolved within the probed depth range. The improved blood compatibility is achieved mainly from the surface chemistry, wettability and nanotopography and not from small differences in stiffness.

3.6. Bacteria adhesion

To evaluate the antibacterial activity of the nanostructured surfaces, all the surfaces were incubated for 6 hours (included in the SI) and 24 hours with *P. aeruginosa* and *S. aureus* bacteria. PS and PCL flat surfaces were used as controls for all bacteria studies. Following the incubation, the live/dead bacteria staining was conducted to assess the amount of bacteria attached to different surfaces. Fig. 6A and S1A (SI) show the fluorescence microscopic images of different surfaces after the incubation periods with *P. aeruginosa*. Fig. S1B, C (SI), 6B and C also show plots quantifying the percentage of area fraction of the surfaces covered by live and dead *P. aeruginosa* bacteria over 6 and 24 hours of incubation periods respectively. Results indicate that there was a significant difference in % of area covered by live *P. aeruginosa*, between PCL and PS during the 6-hours incubation period. But after the 24-hours incubation period, the PCL surfaces were almost 96% covered with live *P. aeruginosa*, similar to the PS surfaces. In contrast to this, all the nanostructured surfaces reduced *P. aeruginosa* attachment in both incubation periods; however, modified NW surfaces exhibited the least adhesion of live *P. aeruginosa* compared to the control surfaces. For instance, after the 24-hours incubation (Fig. 6B), the % area fraction covered with live *P. aeruginosa* on NW_{TN} and $NW_{TN+CMKC}$ were just 0.16% and 0.04% respectively, while NW had 0.42% of live *P. aeruginosa* coverage.

Results also indicate that, compared to PCL surfaces, NW surfaces had significantly higher % area fraction of dead *P. aeruginosa* bacteria during the 6-hours incubation period (Fig. S1C: SI) suggesting that these surfaces were more antibacterial than PCL. However, after the 24-hours incubation period, NW groups had shown a significant reduction in % area fraction of dead *P. aeruginosa*, indicating that these surfaces are not only antibacterial but can also inhibit bacterial adhesion and growth on their surfaces. For instance, after 24-hours incubation (Fig. 6C), $NW_{TN+CMKC}$ had the least % area fraction of dead *P. aeruginosa*, approximately around 10.3%, followed by NW_{TN} with 32% area covered. NWs typically exhibit a unique pillar-like structure creating a complex surface environment, which hinders bacterial adhesion by providing fewer flat surfaces for their attachment. Previous studies have highlighted that the hierarchical structure of PCL NW allows for enhanced interactions with the surrounding environment, which can influence bacteria behavior.[67] Thus, NWs inherent topography has contributed towards creating a less conducive environment for bacterial colonization.

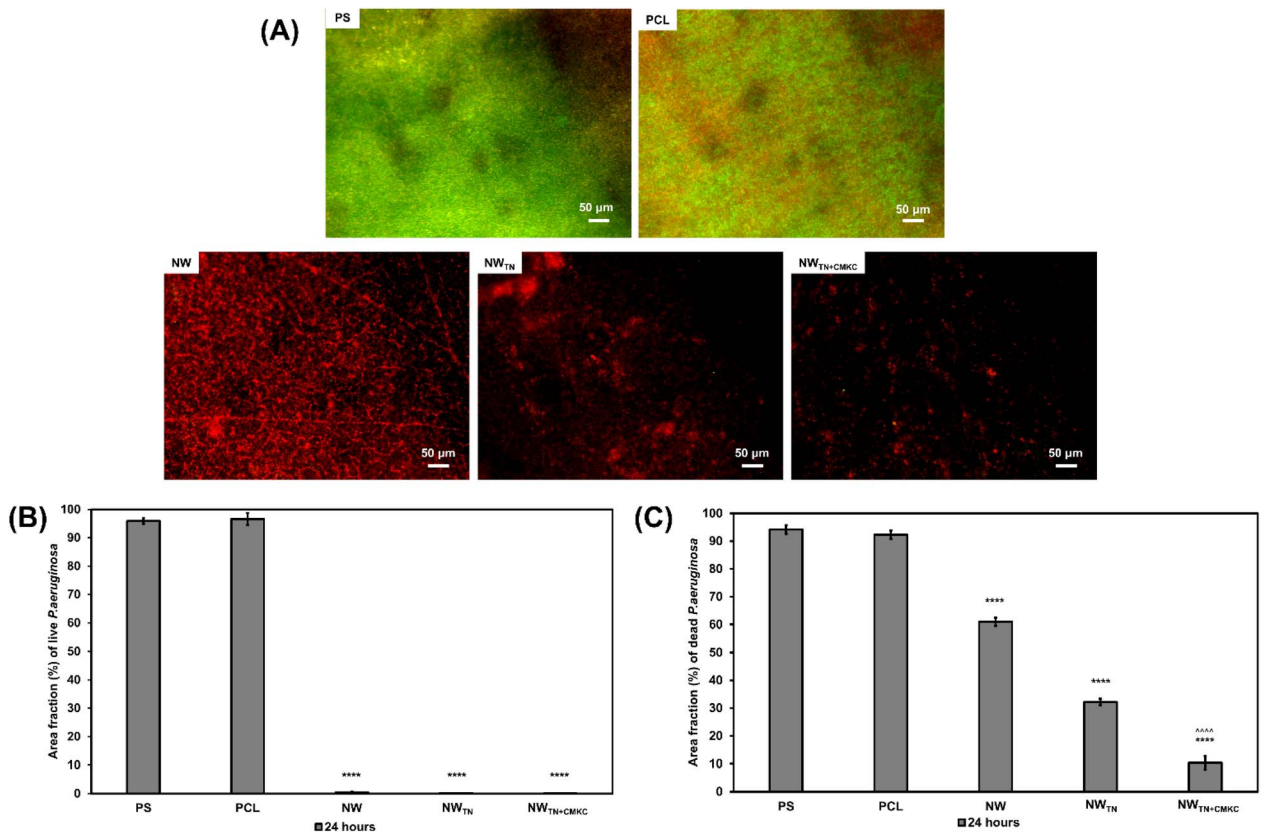

Fig. 6 (A) Representative fluorescence microscopic images of surfaces after 24 hours of incubation with *P. aeruginosa*. The graphs represent the percentage of the area fraction of different surfaces covered by (B) live and (C) dead *P. aeruginosa* bacteria after 24 hours of incubation. **** represent p-value < 0.0001 when compared to PCL control and ^^^^ represent p-value < 0.0001 when compared to NW_{TN}.

Fig. 7A and S2A (SI show the fluorescence microscopic images of different surfaces after the incubation periods with *S. aureus*. Fig. S2B, C (SI), 7B and C also shows plots quantifying the % of area fraction of the surfaces covered by live and dead *S. aureus* bacteria over 6 and 24 hours of incubation periods respectively. Similar to *P. aeruginosa*, live *S. aureus* bacteria attachment was significantly low in NW surfaces compared to PCL surfaces after the 6-hours incubation period. But the % area fraction of live *S. aureus* bacteria increased on the NW surfaces after the 24-hours incubation period. However, unlike NW surfaces, their modified surfaces, with TN and CMKC, exhibited increased antibacterial activity by drastically reducing live *S. aureus* attachment during both the incubation periods. For instance, after 24-hours incubation (Fig. 7B), % area fraction covered by live *S. aureus* on NW_{TN} and $NW_{TN+CMKC}$ were just 0.72% and 0.67% when compared to NW which had 89.32% of live *S. aureus* coverage. Additionally, there was a significant increase in % area fraction of dead *S. aureus* bacteria in all the nanostructured surfaces when compared to PCL surfaces (Fig. 7C). However, the modified NW surfaces exhibited the most % area fraction of dead *S. aureus* bacteria compared to NW surfaces. This validates that NW surfaces, modified with TN and CMKC, exhibited improved antibacterial properties.

The amount of attachment of *S. aureus* bacteria on surfaces is high compared to *P. aeruginosa.* This difference in bacterial adhesion can be attributed to the presence of surface structures like pili and adhesins on the bacteria, which affect their binding effect. *P. aeruginosa* is characterized by its motility and the presence of pili, which are hair-like appendages that facilitate attachment to the surfaces.[68] On the other hand, *S. aureus* possesses a variety of adhesins that enhance its ability to attach to surfaces, including fibronectin-binding proteins and clumping factors.[69,70] These proteins can interact with the material surface enhancing adhesion. *P. aeruginosa*, while also possessing adhesins, tend to rely more on flagella and motility for attachment, which may not be as effective as the adhesive mechanisms employed by *S. aureus.*[71] Another important factor is the relative size of both the bacteria. *S. aureus* is a spherical-shaped bacteria with 0.5 to 1 μm diameter[70] whereas *P. aeruginosa* is a rod-shaped bacterium having length of 1–5 μm and width of 1 μm.[68] Due to this size difference, it is possible for the smaller *S. aureus* to agglomerate and cluster even in tiny spaces and further grow into colonies. Therefore, a substantial difference can be observed in the amount of bacterial adhesion between the two bacteria strains.

Both bacteria show evident stacking up in layers on PS and PCL control surfaces (Fig. 8(A and B), discussed below). These layers account for the combined sum of percentage of areas, covered by their live/dead bacteria, to go above the total 100% of area coverage.

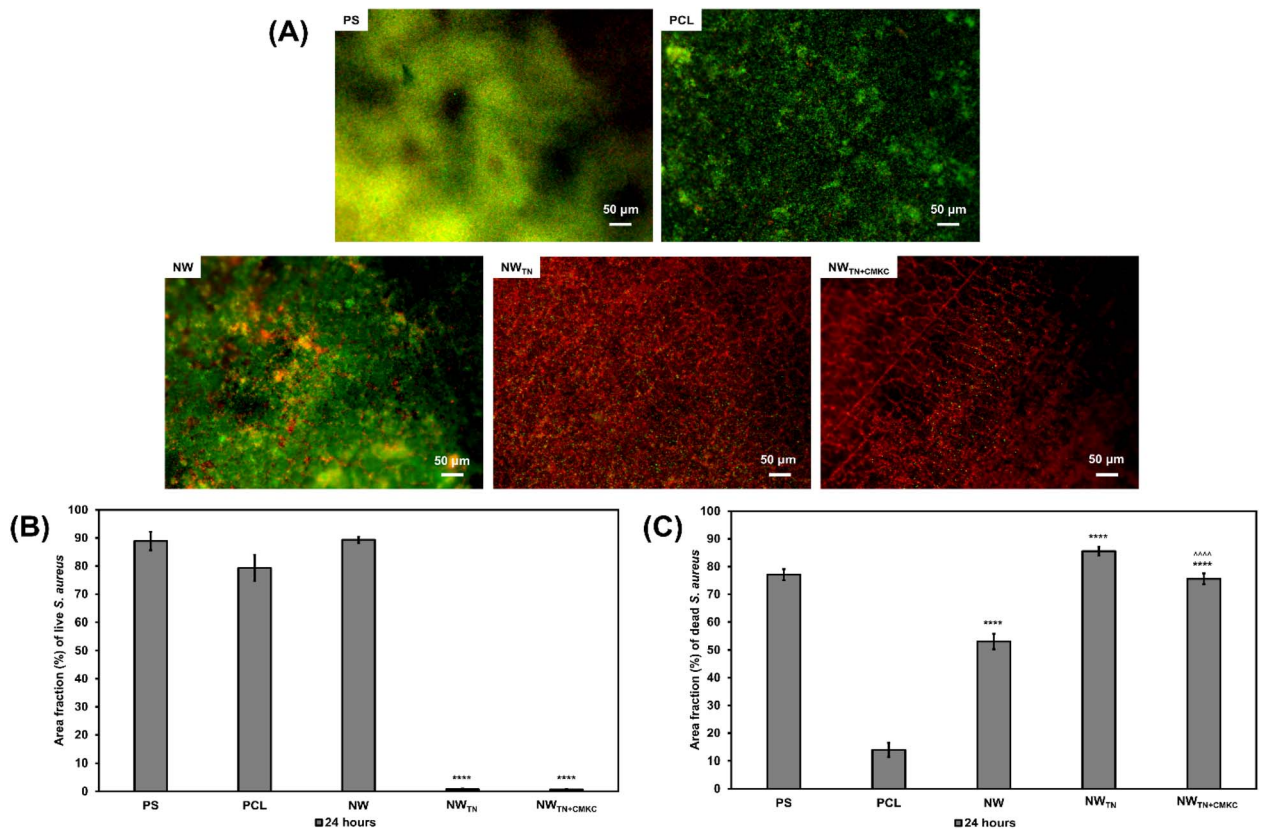

Fig. 7 (A) Representative fluorescence microscopic images of surfaces after 24 hours of incubation with *S. aureus*. The graphs represent the percentage of the area fraction of different surfaces covered by (B) live and (C) dead *S. aureus* bacteria after 24 hours of incubation. **** represent p-value < 0.0001 when compared to PCL control and ^^^^ represent p-value < 0.0001 when compared to NW_{TN}.

3.7. Bacteria morphology

Understanding the morphological changes of viable bacteria on the implant surfaces is vital to determine how bacteria attach, proliferate and form biofilms. SEM images of different surfaces were captured after the bacteria were fixed by following appropriate fixing mechanisms. Fig. S3 (SI) and 8A shows the SEM images of surfaces after 6 and 24 hours of *P. aeruginosa* incubation respectively. Fig. S4 (SI) and 8B show the SEM images of surfaces after 6 and 24 hours of *S. aureus* incubation respectively. Bacteria cells and colonies are false colored in the figures for better visualization and distinction from the topography of the surfaces.

Similar to the results discussed in the previous section, initially the NWs with Gram-negative *P. aeruginosa* exhibited reduced bacterial adhesion on their surfaces compared to the PCL control surfaces, which had more bacterial colonization. However, after the 24-hours incubation period, the modified NW groups tend to show greater inhibition for bacterial adhesion and biofilm formation compared to their control group. Similar results were observed with Gram-positive *S. aureus* bacteria. This is because the incorporation of TN and CMKC onto surfaces significantly enhances their antibacterial properties, primarily due to their unique biochemical interactions with bacterial cells. TN exhibits inherent antimicrobial activity due to its amphoteric nature, allowing it to function as both polycation and polyanion in polyelectrolyte coatings. This duality of TN enables it to effectively disrupt bacterial cell walls and membranes, leading to bacterial cell lysis and death.[33,72] Moreover, the addition of CMKC, known for its biocompatibility and antibacterial properties, complements the action of TN. The negatively charged carboxymethyl groups in CMKC create an electrostatic repulsion between CMKC and the negatively charged surfaces of bacterial cells. This repulsion can disrupt the initial stages of bacterial adhesion, which is the critical step in biofilm formation.[73] The presence of carboxymethyl groups also enhances the solubility and bioactivity of KC, allowing for better interaction with bacterial cells. This interaction can lead to increased permeability of the bacterial cell membrane, resulting in cell lysis and death.[74] In addition to the direct antibacterial effects of CMKC, its antioxidant properties may

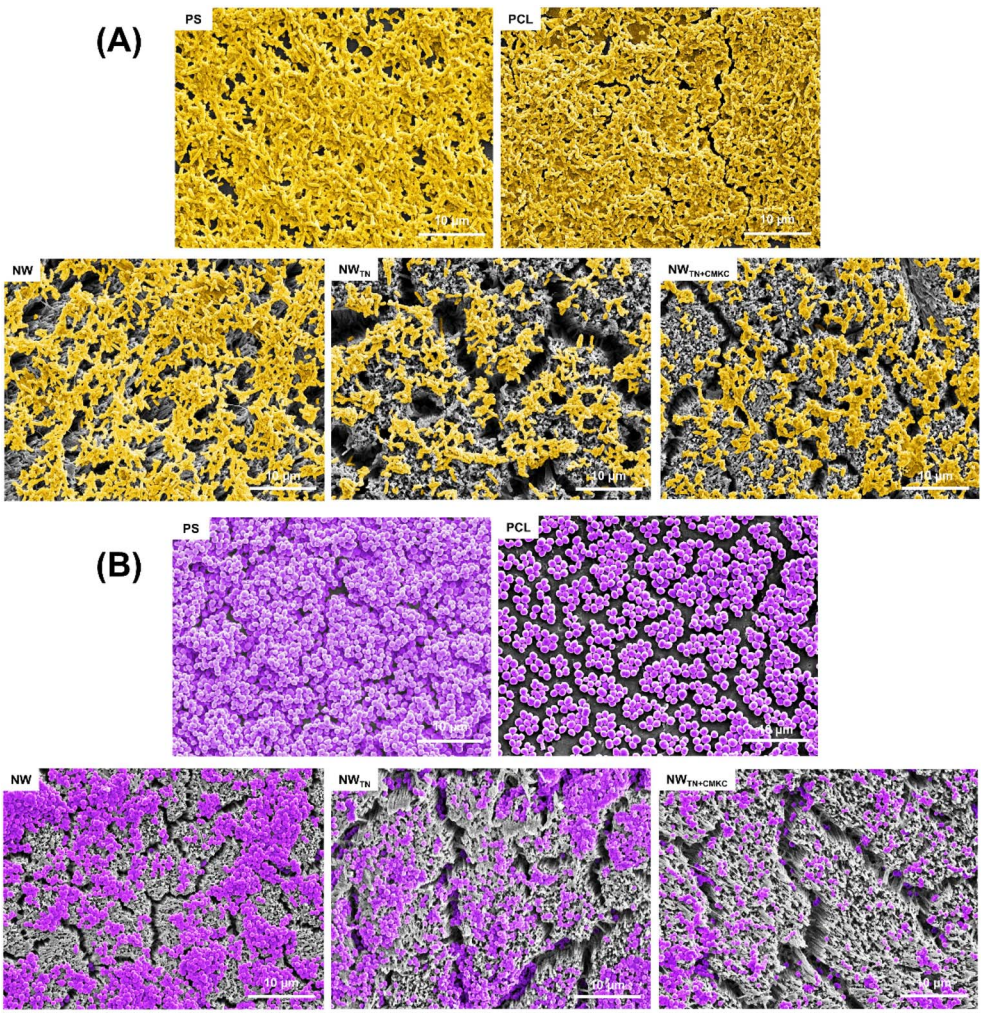

Fig. 8 Representative SEM images of bacteria morphology after 24 hours of (A) *P. aeruginosa* and (B) *S. aureus* incubation captured at 2500× magnification.

also play a crucial role in mitigating bacterial activity. Antioxidants help reduce oxidative stress in the surrounding environment, which can be detrimental to bacteria survival.[30] This synergistic effect attributed to the unique properties of both TN and CMKC helps create an unfavorable environment for bacterial colonization. Therefore, these findings confirmed the improved antibacterial activity of TN and CMKC on PCL nanostructured surfaces.

3.8. Cytotoxicity of different surfaces

In this work, PCL surface's topography and chemistry have been modified and hence, it is crucial to determine whether the surface modifications induce any kind of toxicity to the cells. This is vital to understand if the modified surfaces can be incorporated in the production of BCDs without causing any negative effects.[71,72] Commercially available LDH cytotoxicity assay, which follows a coupled two-step reaction, was utilized to characterize the cytotoxicity of different surfaces. This is particularly important in clinical diagnostics, as increased LDH levels can indicate tissue damage or disease conditions, such as myocardial infarction or various cancers.[75,76] The LDH assay protocol is based on an enzymatic coupling reaction, which plays an important role in cellular metabolism by catalyzing the conversion of lactate to pyruvate. Lactate dehydrogenase (LDH) is a cytosolic enzyme present in many different cell types, which is released into the cell culture medium when the plasma membrane of the cells is damaged. This LDH released from the damaged cells serves as an indicator of the cell membrane integrity and cell viability, thus a measurement of cytotoxicity.[77]

The LDH activity of different surfaces was evaluated (Fig. 9). Polystyrene (PS) was also considered as a standard control for this study. The maximum LDH activity was observed in the negative control (max release) as the erythrocyte cells were lysed intentionally, to release the maximum possible amount of LDH. The positive control (Sp) was prepared by adding erythrocyte suspension to empty wells in the well-plate, which experienced natural cell death due to the interaction with the well-plate surfaces. The LDH activity on the negative control was significantly high compared to all the other surfaces exposed to the erythrocyte cell suspension, including the positive control. This significant difference in LDH activity of all surfaces with respect to the negative control indicated that the physical and chemical modifications done on the surfaces did not cause any cytotoxic effects on the cells.

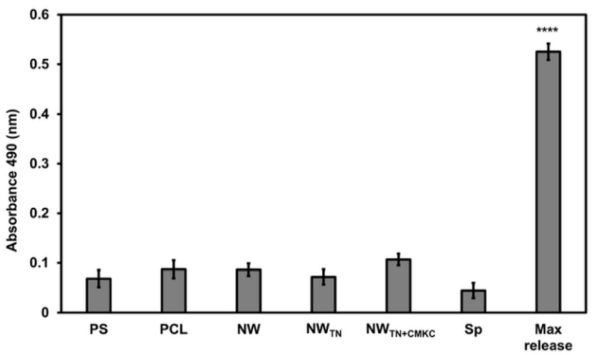

Fig. 9 Cell cytotoxicity for erythrocytes exposed to different surfaces measured using LDH assay. Results indicate that the LDH activity on negative control (100% dead cells) was significantly high (**** represents p-value < 0.0001) compared to the LDH activity on all the surfaces and the positive control (Sp = 100% live cells). Error bars represent the standard deviation.

3.9. Erythrocyte adhesion on different surfaces

Understanding the adhesion properties of erythrocytes on surfaces is required to enhance the designs of biomaterials that can promote optimal hemocompatibility and reduce complications related to blood–material interaction. When erythrocytes adhere to biomaterial surfaces, they initiate a coagulation cascade, which is critical for wound healing and preventing excessive bleeding. Higher levels of erythrocyte adhesion may suggest that a material has favorable interactions with blood components, potentially leading to increased thrombosis, which can be beneficial in hemostatic applications.[78] In contrast, lower erythrocyte adhesion may indicate a non-thrombogenic surface, which is desirable in vascular grafts and stents to prevent thrombosis and ensure long-term patency.[79,80] The balance between promoting adhesion for hemostatic purposes and preventing excessive adhesion to avoid thrombosis is crucial for a biomaterial's design.

Erythrocyte adhesion on different surfaces was characterized by using fluorescence microscopy after 1.5 hours (Fig. S5: SI) and 6 hours of incubation (Fig. 10). Polystyrene (PS) and flat PCL surfaces were used controls for all time points. Results after 6 hours of incubation indicate that the NW surfaces had no significant differences in erythrocyte adhesion when compared with the PCL surfaces. On the other hand, the modified NW surfaces (NW_{TN} and $NW_{TN+CMKC}$) exhibited significantly higher erythrocyte adhesion compared to the NW surfaces. This can be attributed to the addition of TN and CMKC to the surfaces. Incorporation of TN and CMKC increases the hydrophilicity of surfaces which can lead to improved water retention and protein adsorption on the surfaces.[81] Also, the ionic nature of both coatings can lead to enhanced electrostatic interactions with erythrocytes and proteins.[82] Furthermore, erythrocytes require a certain level of rigidity in their substrate for stable attachment to specific adhesion sites, which is provided by the architecture of NW surfaces. The topographical features of NWs can mimic the extracellular matrix (ECM) found in natural tissues.[83] These hierarchical and distributed features allow for a more extensive interaction between erythrocytes and the NW surfaces, leading to enhanced adhesion compared to flat control surfaces. The synergistic effect of these nanostructured topography of the surfaces, modified along with the organic compounds, results in enhanced erythrocyte adhesion.

3.10. Erythrocyte morphology on different surfaces

The unique structure of erythrocytes, characterized by their biconcave shape, maximizes surface area for gas exchange and facilitates their deformability, allowing them to navigate through the narrowest capillaries.[84,85] They are anuclear cells

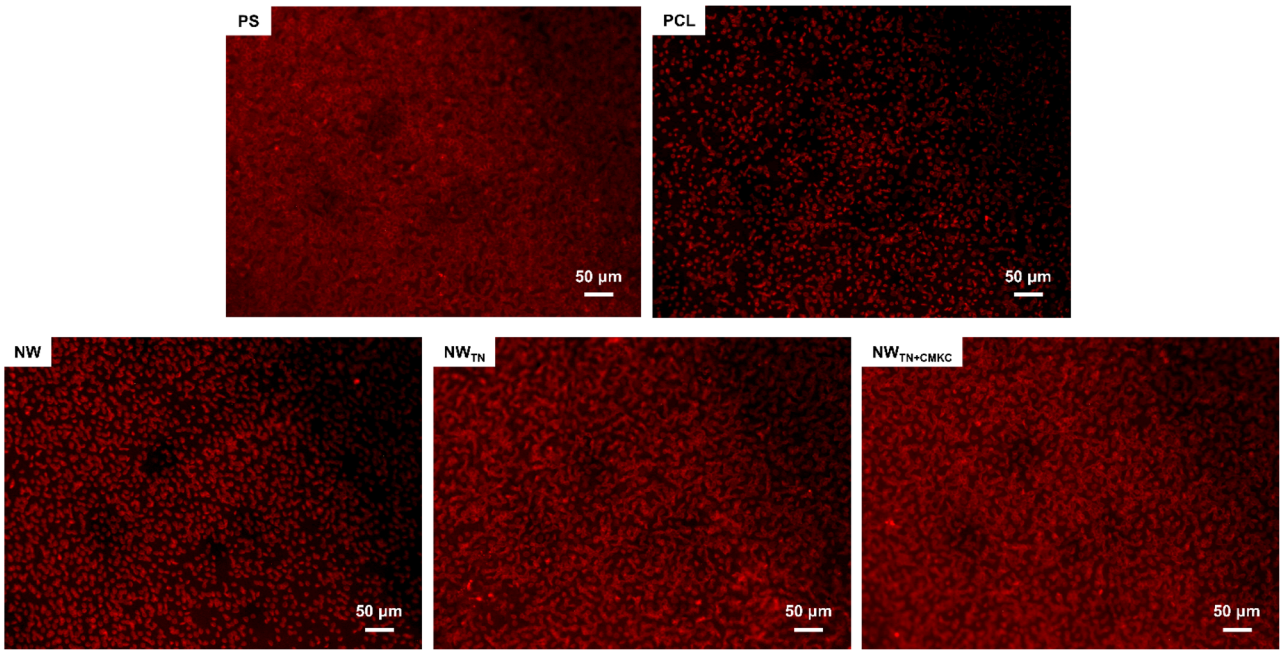

Fig. 10 Representative fluorescence microscopic images of adhered erythrocyte cells on surfaces after 6 hours of incubation.

that contain lipids and proteins, and hemoglobin that binds to oxygen.[86] Identification of erythrocytes with disruptions and abnormalities in their cell morphology serves as a marker for hemolytic pathologies and oxidative damage to integrated membrane proteins.[87,88] Previous studies have reported that there are 18 different types of morphological changes observed in erythrocytes due to different conditions.[89] Few of such disrupted abnormal morphologies of erythrocytes include echinocyte, spherocyte, stomatocyte, sickle cell, *etc.* Each type of these abnormalities corresponds to an associated condition, disease, or deficiency. These cell morphological disruptions compromise erythrocyte's oxygen-carrying ability, which further leads to ischemic conditions.[90,91] Therefore, the capacity of erythrocytes to retain their discocyte, biconcave shape upon adhesion on surfaces is vital for effective blood flow and oxygen delivery, which indicates that the surfaces are capable of supporting normal erythrocyte functionality.[92] Hence, the erythrocyte cell morphology on different surfaces was characterized using SEM. In this work, hemocompatibility is defined by the ability of the surface to preserve the normal erythrocyte morphology and integrity upon contact without inducing any shape changes, rather than by a reduction in the number of adherent cells.

In this study, two types of morphological changes were observed prominently apart from a few others which were not significant. Stomatocytes and different stages of echinocytes were the major morphological changes observed on different surfaces (Fig. 11). Stomatocytes have a mouth-like (stoma) appearance, often associated with alterations in the lipid bilayer of the cell membrane.[93] On the other hand, formation of echinocytes (erythrocytes with spicules) undergoes echinocytosis in which the surface area of the outer lipid monolayer is increased with respect to the inner monolayer. There are different stages of echinocytosis. During stage 1, the normal erythrocyte cell shape is transformed to have several irregularities on its rim. Furthermore, in stage 2, the cells transform into an elliptical body slightly distributed over its surface with different sizes of blunt spicules. Finally, it reaches a sphero-echinocyte morphology, where it is transformed into a sphere with short and sharp spicules. Even though the stomatocytes and initial stages of echinocytes are partially reversible, the sphero-echinocyte is irreversible due to extensive loss of membrane.[94–96]

The SEM imaging results show the morphological changes of erythrocytes adhered to different surfaces after 1.5 hours (Fig. S6: SI) and 6 hours of incubation (Fig. 12A). The percentage

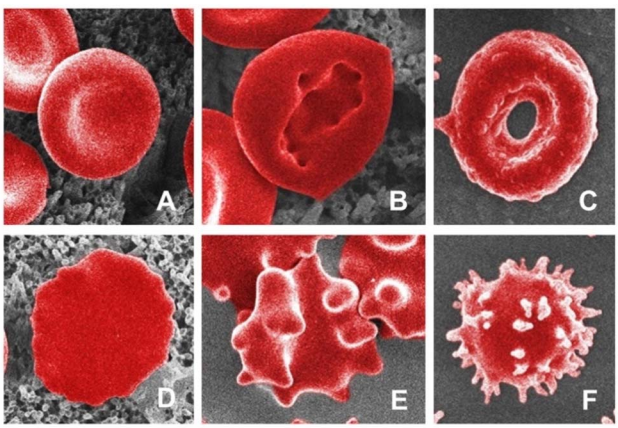

Fig. 11 Representative images illustrating distinct RBC shapes: (A) normal biconcave shape (B) stomatocyte (C) punctured cell membrane with holes being a sign of hemolysis (D) stage 1 echinocyte (E) stage 2 echinocyte (F) sphero-echinocyte. Images are illustrative only and are not associated to a specific surface.

of cell change on different surfaces was calculated from the SEM images and plotted as shown in Fig. 12B. PS was used as a control to monitor the morphology of erythrocytes. Results indicate that after 6 hours of incubation, PCL surfaces exhibited a drastic increase in the percentage of cell change, approximately equal to 95%, while PS surfaces had 100% cell change documented. This result can be correlated with Fig. 12A, where PS surfaces were completely filled with sphero-echinocytes, while PCL surfaces exhibited multiple morphological changes like echinocytes, stomatocytes and punctured cell structures with holes, which are an indication of hemolysis.[97] NW surfaces have shown similar results as PCL after 1.5 and 6 hours with relatively more stomatocytes than echinocytes (Fig. S6 and 12). No sphero-echinocytes were observed on NW surfaces unlike PS and PCL surfaces. However, NW_{TN} and $NW_{TN+CMKC}$ had a greater number of healthy erythrocyte cells, with the normal biconcave shape, as opposed to its control NW surfaces. After 6 hours of incubation, % cell change in NW_{TN} was 26.2% and in $NW_{TN+CMKC}$ was 31.7%, which were still significantly lower compared to their control surfaces. Even this reduced % cell change contained only early stages of echinocytes and stomatocytes, and no sphero-echinocytes.

The PS surfaces exhibited expected results with respect to previous literature.[98] The morphological changes of cells on PCL surfaces can be attributed to the physiochemical interactions between the cell membrane and PCL material, which can disrupt the lipid bilayer's integrity and alter the membrane's mechanical properties. The primary issue with PCL surfaces is its hydrophobicity that leads to poor protein adsorption, which is essential for the initial stages of blood–material interaction.

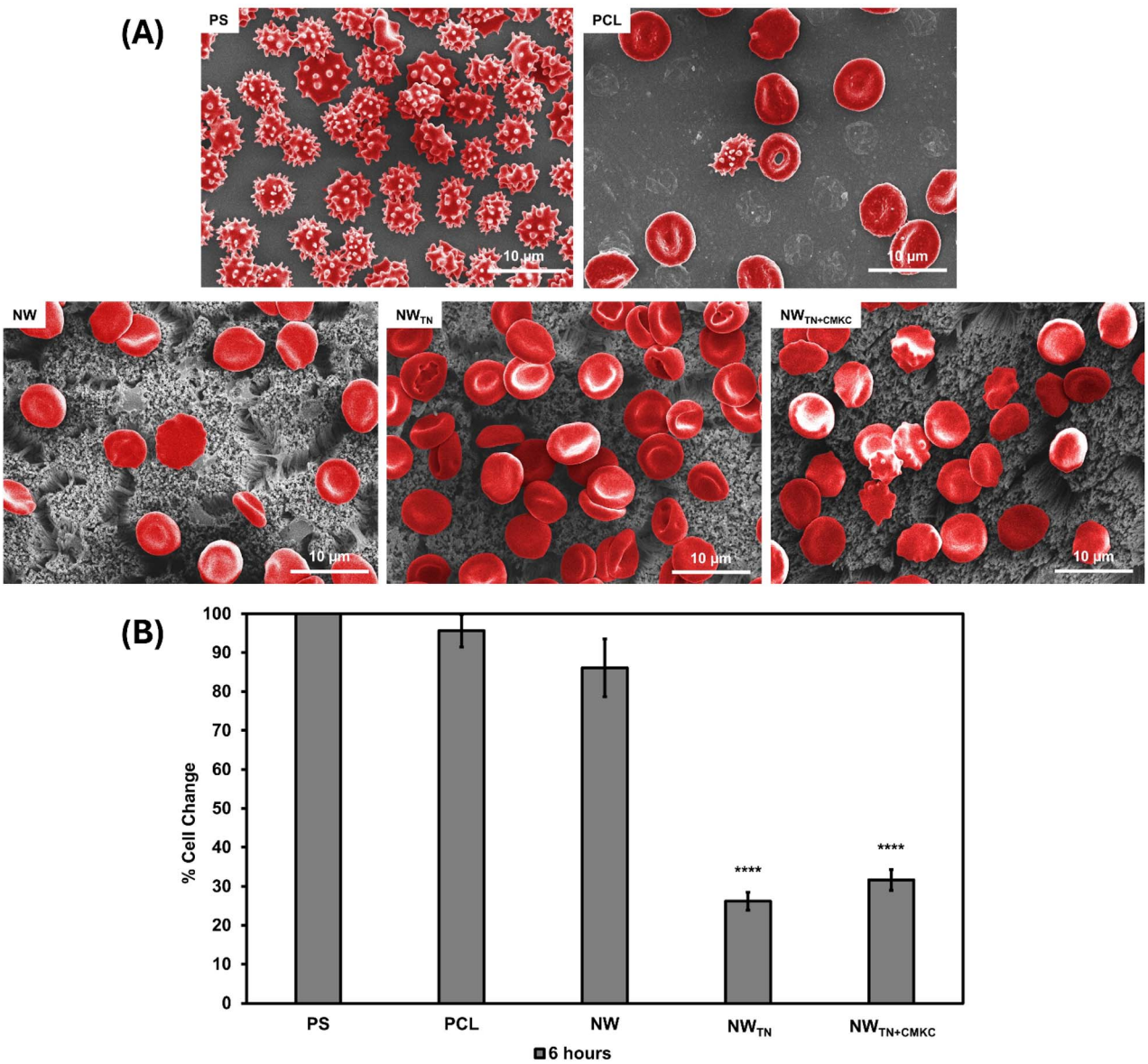

Fig. 12 (A) Representative SEM images depicting erythrocyte cells morphological changes on surfaces after 6 hours of incubation (2500× magnification). (B) Percentage of morphological changes in erythrocytes on different surfaces after 6 hours of incubation, characterized from SEM images. Error bars represent standard deviation. **** represent p-value < 0.0001 when compared to PCL control.

Even though PCL surfaces exhibit good biocompatibility with certain cells, their hemocompatibility is poor due to insufficient protein adsorption and subsequent platelet activation, which are highly influenced by the surface wettability.[99]

The topography and wettability of the NW surfaces influence the cell interactions. Previous studies indicate that PCL NWs, due to their distinct morphology and topography, may facilitate a more optimal interaction with blood components, potentially leading to lower platelet activation and aggregation.[100–102] These findings align with the results of this study, where NW surfaces exhibited slightly reduced morphological changes in erythrocytes, compared to the PS and PCL control surfaces.

Furthermore, the addition of TN and CMKC on these nanostructured surfaces exhibited a significantly drastic impact on retaining the morphology of adhered erythrocytes. This can be attributed to the synergistic effect provided by both physical and chemical modifications done on these surfaces, which enhanced erythrocyte cell compatibility. The hydrophilic nature of TN and the functional properties of CMKC, combined with nanostructured surfaces, create a more stable microenvironment for erythrocytes.[81,103] Also, previous studies have shown that incorporation of antioxidant supplements have significantly improved the erythrocyte membrane integrity by reducing oxidative lesions and membrane lipid peroxidation.[104–106] For instance, ascorbic acid's antioxidant properties has shown promising results in reducing erythrocyte membrane fragility and decreased hemolysis as they help maintain hemoglobin in a reduced state and minimizing erythrocyte oxidative injury.[107,108] The results with TN and CMKC can be correlated to findings on ascorbic acid suggesting a structural–functional relationship between them. The presence of antioxidant functional groups such as phenolic rings in TN and sulfate/carboxyl moieties in CMKC can be correlated with the redox activity of ascorbic acid, contributing to reduction in osmotic fragility and membrane stability.[30,109,110] This enhanced environment helps the cells to maintain its structural integrity and functionality and thus reducing the likelihood of hemolysis. However, no statistically significant % cell change was observed between NW_{TN} and $NW_{TN+CMKC}$ surfaces.

4. Conclusions

In this study, PCL nanostructured surfaces (NW) were fabricated and modified with organic compounds, such as TN and CMKC, for investigating their material properties, antibacterial properties and influence on erythrocyte integrity. The morphology of the surfaces was analyzed (SEM) and revealed the topographical differences between the nanostructured surfaces and the flat PCL control surfaces. There was no significant difference in the morphology of the surfaces post modification with TN and CMKC. Surface wettability analysis (Contact angle) has shown that NW and modified NW surfaces were hydrophilic in contrast to their hydrophobic PCL control surfaces. Surface chemistry analysis (XPS) revealed peaks of nitrogen and sulphur in TN modified and CMKC modified groups respectively, compared to unmodified surfaces. These results account for the presence of amine groups in TN and presence of sulphate groups in CMKC, which indicated the successful modification of the nanostructured surfaces. Surface crystallinity analysis (XRD) was conducted, and the results exhibited no significant differences in the patterns between PCL control, NW and modified NW surfaces. Mechanical properties of surfaces, such as indentation hardness and elastic modulus, were analyzed using nano-indentation technique. Results indicated that NW surfaces have enhanced load bearing capacity and thus increased durability and flexibility.

Following the fabrication and modification of surfaces, PCL nanostructured surfaces were subjected to Gram-positive (*S. aureus*) and Gram-negative (*P. aeruginosa*) bacterial strains, at two different incubation periods, to understand the antibacterial properties of different surfaces. The surfaces were characterized by bacteria adhesion to evaluate the amount of live or dead bacteria and bacteria morphology to understand the morphological changes or biofilm formation of the cells. The percentage area fraction coverage of live and dead bacteria was also calculated. It was observed that nanostructured surfaces modified with TN and CMKC exhibited improved antibacterial properties by reducing bacterial adhesion and inhibiting biofilm formation. This can be attributed to the synergistic effect of nanostructures combined with organic compounds. Modified NW surfaces exhibited the least % of area covered by bacteria.

Furthermore, nanostructured surfaces were evaluated to understand their effects on erythrocyte integrity and viability. Cytotoxicity assay was conducted to assess if the surface modifications have induced any toxicity towards adhered cells. Results have shown significantly low LDH activity on all the surfaces when compared to the negative control, indicating that the physical and chemical modifications done on the surfaces did not induce any cytotoxic effects on the cells. Surfaces were characterized for erythrocyte adhesion using fluorescence microscopy, to assess their viability towards erythrocytes. Modified NW surfaces exhibited increased erythrocyte adhesion compared to their control surfaces, which can be attributed to the synergistic effect of addition of TN and CMKC along with nanostructured surfaces. Erythrocyte morphology was examined using SEM and the results indicated that the modified NW surfaces significantly retained the healthy erythrocyte morphology and integrity than their control surfaces. This can be attributed to the antioxidant properties of both TN and CMKC which helps in reducing the oxidative injuries of the erythrocytes. No significant differences were observed between the NW_{TN} and $NW_{TN+CMKC}$ surfaces in terms of maintaining erythrocyte cell integrity, but the $NW_{TN+CMKC}$ surfaces had improved antibacterial properties.

These findings indicate that PCL nanostructured surfaces coupled with organic compounds like TN and CMKC can provide a stable biocompatible environment for cell integrity and serve as a better alternative for BCDs.

Author contributions

V. S. (Vignesh Sathyanarayanan): conceptualization, methodology, validation, formal analysis, investigation, data curation,

visualization, writing – original draft, writing – review & editing. B. L. P (Bruno Leandro Pereira): investigation, formal analysis, data curation. L. C. M. (Liszt Coutinho Madruga): conceptualization, formal analysis, validation, project administration, writing – review & editing. P.S. (Paulo Soares): resources, supervision, formal analysis. K. C. P. (Ketul C. Popat): conceptualization, validation, writing – review & editing, supervision, project administration, resources, funding acquisition.

Conflicts of interest

The authors have no conflicts of interest to declare.

Data availability

Due to the large amount of data related to the study results it is not possible to upload all the data to the public network, however, some data is included in supplementary information (SI) and more data is available upon request. Supplementary information is available. See DOI: **https://doi.org/10.1039/d5ra05152e**.

Acknowledgements

The authors wish to thank the Analytical Resources Core (RRID: SCR_021758) at Colorado State University for instrument access, training, and assistance with data acquisition for SEM and XPS. V.S. would also like to thank Rebecca Miller, Somayeh Baghersad, Fernanda R Veregue, Abhishek Bhattacharjee and Aniruddha Vijay Savargaonkar for their support in training and technical guidance in specific experimental procedures that were essential to this research. This research was funded by National Institutes of Health (NIH), grant number 1R21EB033511-01 and National Science Foundation (NSF), grant number 233878.

References

1 I. H. Jaffer and J. I. Weitz, *Acta Biomater.*, 2019, **94**, 2–10.
2 M. Weber, H. Steinle, S. Golombek, L. Hann, C. Schlensak, H. P. Wendel and M. Avci-Adali, *Front. Bioeng. Biotechnol.*, 2018, **6**, 395774.
3 W. Zingg, A. Barton, J. Bitmead, P. Eggimann, M. Pujol, A. Simon and J. Tatzel, *Infect. Prev. Pract.*, 2023, **5**, 100271.
4 T. J. Vachharajani, J. J. Taliercio and E. Anvari, *Am. J. Kidney Dis.*, 2021, **78**, 116–124.
5 R. Tramm, D. Ilic, A. R. Davies, V. A. Pellegrino, L. Romero and C. Hodgson, *Cochrane Database Syst. Rev.*, 2015, **2015**, CD010381.
6 A. Bhattacharjee, A. V. Savargaonkar, M. Tahir, A. Sionkowska and K. C. Popat, *RSC Adv.*, 2024, **14**, 7440–7458.
7 X. Hu, T. Wang, F. Li and X. Mao, *RSC Adv.*, 2023, **13**, 20495.
8 S. Rogers and A. Doctor, *Crit. Care Clin.*, 2020, **36**, 267.
9 S. Alibeik and K. N. Sask, in *Functional Biopolymers*, eds. M. A. Jafar Mazumder, H. Sheardown and A. Al-Ahmed, Springer International Publishing, Cham, 2019, pp. 149–189.
10 M. Weber, H. Steinle, S. Golombek, L. Hann, C. Schlensak, H. P. Wendel and M. Avci-Adali, *Front. Bioeng. Biotechnol.*, 2018, **6**, 395774.
11 J. Kuchinka, C. Willems, D. V. Telyshev and T. Groth, *Bioengineering*, 2021, **8**, 215.
12 A. Bhattacharjee, A. V. Savargaonkar, M. Tahir, A. Sionkowska and K. C. Popat, *RSC Adv.*, 2024, **14**, 7440–7458.
13 N. Altın, C. H. Hekimoğlu, T. U. Ulusoy, S. Kuzi, G. Sevinç, A. Tekin, B. R. Aksoy, I. Şencan, N. A. Sr, C. H. Hekimoğlu, T. U. Ulusoy, S. Kuzi, G. Sevinç, A. Tekin, B. R. Aksoy and İ. Şencan, *Cureus*, 2024, **16**(4), e57720.
14 B. Rha, I. See, L. Dunham, P. K. Kutty, L. Moccia, I. W. Apata, J. Ahern, S. Jung, R. Li, J. Nadle, S. Petit, S. M. Ray, L. H. Harrison, C. Bernu, R. Lynfield, G. Dumyati, M. Tracy, W. Schaffner, D. C. Ham, S. S. Magill, E. N. O'Leary, J. Bell, A. Srinivasan, L. C. McDonald, J. R. Edwards and S. Novosad, *MMWR Morb. Mortal. Wkly. Rep.*, 2023, **72**, 153–159.
15 V. Leszczak and K. C. Popat, *ACS Appl. Mater. Interfaces*, 2014, **6**, 15913–15924.
16 A. Azari, A. Golchin, M. M. Maymand, F. Mansouri and A. Ardeshirylajimi, *Adv. Pharm. Bull.*, 2021, **12**, 658.
17 W. S. Jeong, Y. C. Kim, J. C. Min, H. J. Park, E. J. Lee, J. H. Shim and J. W. Choi, *Polymers*, 2022, **14**, 740.
18 F. C. Menezes, N. M. Siqueira, S. Fung, J. M. Scheibel, D. J. Moura, M. Guvendiren, J. Kohn and R. M. D. Soares, *Polym. Adv. Technol.*, 2022, **33**, 2682–2695.
19 H. K. Kim, S. J. Jang, Y. S. Cho and H. H. Park, *Polymers*, 2022, **14**, 5527.
20 J. Jenkins, J. Mantell, C. Neal, A. Gholinia, P. Verkade, A. H. Nobbs and B. Su, *Nat. Commun.*, 2020, **11**(1), 1–14.
21 E. P. Ivanova, D. P. Linklater, M. Werner, V. A. Baulin, X. M. Xu, N. Vrancken, S. Rubanov, E. Hanssen, J. Wandiyanto, V. K. Truong, A. Elbourne, S. Maclaughlin, S. Juodkazis and R. J. Crawford, *Proc. Natl. Acad. Sci. U. S. A.*, 2020, **117**, 12598–12605.
22 V. Leszczak, D. A. Baskett and K. C. Popat, *J. Biomed. Nanotechnol.*, 2015, **11**, 1080–1092.
23 V. Leszczak, D. A. Baskett and K. C. Popat, *J. Funct. Biomater.*, 2014, **5**, 58–77.
24 V. Leszczak and K. C. Popat, *ACS Appl. Mater. Interfaces*, 2014, **6**, 15913–15924.
25 V. Leszczak, B. S. Smith and K. C. Popat, *J. Biomater. Sci. Polym. Ed.*, 2013, **24**, 1529–1548.
26 S. Baghersad, L. Y. C. Madruga, A. F. Martins, K. C. Popat and M. J. Kipper, *J. Funct. Biomater.*, 2023, **14**, 554.
27 V. K. Manivasagam, R. M. Sabino, P. Kantam and K. C. Popat, *Mater. Adv.*, 2021, **2**, 5824–5842.
28 R. M. Sabino, K. Kauk, L. Y. C. Madruga, M. J. Kipper, A. F. Martins and K. C. Popat, *J. Biomed. Mater. Res., Part A*, 2020, **108**, 992–1005.
29 P. Li, R. Yin, J. Cheng and J. Lin, *Int. J. Mol. Sci.*, 2023, **24**, 11680.

30 L. Y. C. Madruga, R. M. Sabino, E. C. G. Santos, K. C. Popat, R. de C. Balaban and M. J. Kipper, *Int. J. Biol. Macromol.*, 2020, **152**, 483–491.
31 S. Abbasi-Ravasjani, H. Seddiqi, A. Moghaddaszadeh, M. E. Ghiasvand, J. Jin, E. Oliaei, R. G. Bacabac and J. Klein-Nulend, *Front. Bioeng. Biotechnol.*, 2022, **10**, 957263.
32 V. Leszczak, B. S. Smith and K. C. Popat, *J. Biomater. Sci. Polym. Ed.*, 2013, **24**, 1529.
33 S. Baghersad, L. Y. C. Madruga, A. F. Martins, K. C. Popat and M. J. Kipper, *J. Funct. Biomater.*, 2023, **14**, 554.
34 Y. T. Hameed, A. Idris, S. A. Hussain, N. Abdullah and H. Che Man, *J. Environ. Chem. Eng.*, 2020, **8**, 103679.
35 R. M. Sabino, K. Kauk, L. Y. C. Madruga, M. J. Kipper, A. F. Martins and K. C. Popat, *J. Biomed. Mater. Res., Part A*, 2022, **108**(4), 992–1005.
36 L. Y. C. Madruga, K. C. Popat, R. C. Balaban and M. J. Kipper, *Carbohydr. Polym.*, 2021, **273**, 118541.
37 H. Y. Lo, H. T. Kuo and Y. Y. Huang, *Artif. Organs*, 2010, **34**, 648–653.
38 T. Raimondo, S. Puckett and T. J. Webster, *Int. J. Nanomed.*, 2010, **5**, 647–652.
39 N. A. Trujillo and K. C. Popat, *Materials*, 2014, **7**, 2605–2630.
40 S. L. Bechara, A. Judson and K. C. Popat, *Biomaterials*, 2010, **31**, 3492–3501.
41 J. R. Porter, A. Henson and K. C. Popat, *Biomaterials*, 2009, **30**, 780–788.
42 C. Pulletikurthi, N. Munroe, D. Stewart, W. Haider, S. Amruthaluri, R. Rokicki, M. Dugrot and S. Ramaswamy, *J. Biomed. Mater. Res., Part B*, 2015, **103**, 1366–1374.
43 A. P. Khandwekar, D. P. Patil, Y. Shouche and M. Doble, *J. Biomater. Appl.*, 2011, **26**, 227–252.
44 K. Shaikh, W. A. Khan, Md. S. N. Kazi and M. N. M. Zubir, *Nanocellulose: Fundaments and Applications*, 2024, DOI: **10.5772/INTECHOPEN.114221**.
45 Y. Kelvii Kwok, in *21st Century Surface Science - a Handbook*, IntechOpen, 2020.
46 H. Puliyalil, G. Filipič, U. Cvelbar, H. Puliyalil, G. Filipič and U. Cvelbar, *Surface Energy*, 2015, DOI: **10.5772/60852**.
47 G. Yang, H. Lin, B. B. Rothrauff, S. Yu and R. S. Tuan, *Acta Biomater.*, 2016, **35**, 68–76.
48 H. N. Patel, R. Garcia, C. Schindler, D. Dean, S. M. Pogwizd, R. Singh, Y. K. Vohra and V. Thomas, *Polym. Int.*, 2015, **64**, 547–555.
49 K. Du and Z. Gan, *ACS Appl. Mater. Interfaces*, 2012, **4**, 4643–4650.
50 V. Leszczak, D. A. Baskett and K. C. Popat, *J. Funct. Biomater.*, 2014, (5), 58–77.
51 A. G. Namboodiri and R. Parameswaran, *J. Appl. Polym. Sci.*, 2013, **129**, 2280–2286.
52 L. Ye, X. Wu, H. Y. Duan, X. Geng, B. Chen, Y. Q. Gu, A. Y. Zhang, J. Zhang and Z. G. Feng, *J. Biomed. Mater. Res., Part A*, 2012, **100A**, 3251–3258.
53 P. Louette, F. Bodino and J.-J. Pireaux, *Surf. Sci. Spectra*, 2005, **12**, 27–31.
54 M. A. Hamdan, K. N. Mohd Amin and F. Adam, *Food Chem.*, 2024, **452**, 139556.
55 Z. Li, Y. Guo, X. Wang, P. Li, W. Ying, D. Chen, X. Ma, Z. Deng and X. Peng, *ACS Appl. Mater. Interfaces*, 2019, **11**, 34039–34045.
56 N. Shrgawi, I. J. Shamsudin, H. Hanibah, S. A. M. Noor and N. Kasim, *Solid State Phenom.*, 2021, **317**, 327–332.
57 T. T. M. Ho, K. E. Bremmell, M. Krasowska, D. N. Stringer, B. Thierry and D. A. Beattie, *Soft Matter*, 2015, **11**, 2110–2124.
58 E. Gea Rodi, C. Mangeon, E. Dessauw, V. Sansalone, T. Lemaire, E. Renard and V. Langlois, *ACS Sustain. Chem. Eng.*, 2016, **4**, 5475–5482.
59 H. S. Barud, S. J. L. Ribeiro, C. L. P. Carone, R. Ligabue, S. Einloft, P. V. S. Queiroz, A. P. B. Borges and V. D. Jahno, *Polímeros*, 2013, **23**, 135–142.
60 R. Othman, G. T. Vladisavljević, Z. K. Nagy and R. G. Holdich, *Langmuir*, 2016, **32**, 10685–10693.
61 M. P. Motloung, V. Ojijo, J. Bandyopadhyay and S. S. Ray, *J. Appl. Polym. Sci.*, 2020, **137**, 48665.
62 A. Hasan, S. Soliman, F. El Hajj, Y. T. Tseng, H. C. Yalcin and H. E. Marei, *Sci. Rep.*, 2018, **8**, 1–13.
63 L. A. Can-Herrera, A. I. Oliva, M. A. A. Dzul-Cervantes, O. F. Pacheco-Salazar and J. M. Cervantes-Uc, *Polymers*, 2021, **13**, 662.
64 Y. Zhang, X. Wang, Y. Zhang, Y. Liu, D. Wang, X. Yu, H. Wang, Z. Bai, Y. C. Jiang, X. Li, W. Zheng and Q. Li, *ACS Biomater. Sci. Eng.*, 2021, **7**, 4959–4970.
65 F. Sharifi, B. B. Patel, A. K. Dzuilko, R. Montazami, D. S. Sakaguchi and N. Hashemi, *Biomacromolecules*, 2016, **17**, 3287–3297.
66 M. Bontempi, G. Marchiori, M. Petretta, R. Capozza, B. Grigolo, G. Giavaresi and A. Gambardella, *Biomimetics*, 2023, **8**, 617.
67 K. Du and Z. Gan, *ACS Appl. Mater. Interfaces*, 2012, **4**, 4643–4650.
68 S. P. Diggle and M. Whiteley, *Microbiology*, 2020, **166**, 30–33.
69 C. Na, C. J. McNamara, N. R. Konkol, K. A. Bearce, R. Mitchell and S. T. Martin, *Ann. Microbiol.*, 2010, **60**, 495–502.
70 L. G. Harris, S. J. Foster, R. G. Richards, P. Lambert, D. Stickler and A. Eley, *Eur. Cell. Mater.*, 2002, **4**, 39–60.
71 J. A. Pointon, W. D. Smith, G. Saalbach, A. Crow, M. A. Kehoe and M. J. Banfield, *J. Biol. Chem.*, 2010, **285**, 33858–33866.
72 R. Singh, Y. C. Madruga, A. Savargaonkar, A. F. Martins, M. J. Kipper, K. C. Popat, R. Singh, A. Savargaonkar, K. C. Popat, L. Y. C. Madruga, A. F. Martins and M. J. Kipper, *Adv. Mater. Interfaces*, 2024, 2400406.
73 S. Javadiyan, C. M. Cooksley, G. S. Bouras, S. S. T. Kao, C. A. Bennett, P. J. Wormald, S. Vreugde and A. J. Psaltis, *Int. Forum Allergy Rhinol.*, 2022, **12**, 302–305.
74 M. Khodadadi Yazdi, F. Seidi, A. Hejna, P. Zarrintaj, N. Rabiee, J. Kucinska-Lipka, M. R. Saeb and S. A. Bencherif, *ACS Appl. Bio Mater.*, 2024, **7**, 4193–4230.
75 L. Zhou, Z. Xie, Z. Shao, W. Chen, H. Xie, X. Cui, G. Qin and N. Zhao, *J. Thorac. Dis.*, 2018, **10**, 1043–1049.

76 claresta diella, N. Mudjihartini, D. Sunardi, D. N. Chandra, Y. Yulhasri and A. M. Jayusman, *World Nutrition J.*, 2019, **2**, 1–8.
77 S. Kaja, A. J. Payne, Y. Naumchuk and P. Koulen, *Curr. Protoc. Toxicol.*, 2017, **72**, 2.26.1–2.26.10.
78 L. Teng, Z. Shao, Q. Bai, X. Zhang, Y. S. He, J. Lu, D. Zou, C. Feng and C. M. Dong, *Adv. Funct. Mater.*, 2021, **31**, 2105628.
79 J. T. Horobin, S. Sabapathy and M. J. Simmonds, *Artif. Organs*, 2017, **41**, 1017–1025.
80 O. K. Baskurt and H. J. Meiselman, *Clin. Hemorheol. Microcirc.*, 2013, **53**, 23–37.
81 S. Ilanlou, M. Khakbiz, G. Amoabediny, J. Mohammadi and H. Rabbani, *J. Biomed. Mater. Res., Part A*, 2019, **107**, 1690–1701.
82 S. Abbasi-Ravasjani, H. Seddiqi, A. Moghaddaszadeh, M. E. Ghiasvand, J. Jin, E. Oliaei, R. G. Bacabac and J. Klein-Nulend, *Front. Bioeng. Biotechnol.*, 2022, **10**, 957263.
83 K. Y. Baik, S. Y. Park, S. Namgung, D. Kim, D. guk Cho, M. Lee and S. Hong, *Nano Convergence*, 2014, **1**, 1–10.
84 C. S. Olver, *Schalm's Veterinary Hematology*, 7th edn, 2020, 158–165.
85 V. V. Revin, N. V. Gromova, E. S. Revina, N. A. Mel'Nikova, L. A. Balykova, I. N. Solomadin, A. Y. Tychkov, N. V. Revina, O. Y. Gromova, I. V. Anashkina and V. A. Yakushkin, *BioMed Res. Int.*, 2015, **2015**, 973973.
86 M. Diez-Silva, M. Dao, J. Han, C. T. Lim and S. Suresh, *MRS Bull.*, 2010, **35**, 382–388.
87 F. A. Ansari, S. N. Ali and R. Mahmood, *Toxicol. in Vitro*, 2015, **29**, 1878–1886.
88 J. G. Mohanty, E. Nagababu and J. M. Rifkind, *Front. Physiol.*, 2014, **5**, 75882.
89 H. S. Virk and K. C. Popat, *In Vitro Models*, 2022, **1**, 347–363.
90 D. Kouroupis, T. G. Baboolal, E. Jones and P. V. Giannoudis, *J. Orthop. Res.*, 2013, **31**, 1950–1958.
91 N. Alexandre, E. Costa, S. Coimbra, A. Silva, A. Lopes, M. Rodrigues, M. Santos, A. C. Maurício, J. D. Santos and A. L. Luís, *J. Biomed. Mater. Res., Part A*, 2015, **103**, 1366–1379.
92 W. Huang, S. Cheng, X. Wang, Y. Zhang, L. Chen and L. Zhang, *Adv. Funct. Mater.*, 2021, **31**, 2009189.
93 G. Lim H. W., M. Wortis and R. Mukhopadhyay, *Soft Matter*, 2009, **4**, 83–139.
94 H. Xia, G. Khanal, B. C. Strachan, E. Vörös, N. Z. Piety, S. C. Gifford and S. S. Shevkoplyas, *Blood Transfus.*, 2017, **15**, 463.
95 M. U. Martínez-Martínez, L. M. D. G. Llamazares-Azuara, D. Martínez-Galla, P. B. Mandeville, F. Valadez-Castillo, S. Román-Acosta, J. A. Borjas-García and C. Abud-Mendoza, *Lupus*, 2017, **26**, 580–587.
96 K. Sanford, B. J. Fisher, E. Fowler, A. A. Fowler and R. Natarajan, *Antioxidants*, 2017, **6**, 55.
97 I. Mustafa, A. Al Marwani, K. Mamdouh Nasr, N. Abdulla Kano and T. Hadwan, *BioMed Res. Int.*, 2016, **2016**, 4529434.
98 P. Wong, *J. Theor. Biol.*, 2005, **233**, 127–135.
99 L. Liu, S. Guo, J. Chang, C. Ning, C. Dong and D. Yan, *J. Biomed. Mater. Res., Part B*, 2008, **87B**, 244–250.
100 V. Leszczak, B. S. Smith and K. C. Popat, *J. Biomater. Sci. Polym. Ed.*, 2013, **24**, 1529–1548.
101 V. Leszczak and K. C. Popat, *ACS Appl. Mater. Interfaces*, 2014, **6**, 15913–15924.
102 H. B. Hagh, L. D. Unsworth, F. Doustdar and A. Olad, *Polym. Adv. Technol.*, 2023, **34**, 1671–1685.
103 R. M. Sabino, K. Kauk, L. Y. C. Madruga, M. J. Kipper, A. F. Martins and K. C. Popat, *J. Biomed. Mater. Res., Part A*, 2020, **108**, 992–1005.
104 R. Soumya and R. Vani, *Acta Haematol. Pol.*, 2017, **48**, 350–356.
105 A. T. Anastasiadi, K. Stamoulis, A. G. Kriebardis and V. L. Tzounakas, *Front. Physiol.*, 2024, **15**, 1499308.
106 K. Sanford, B. J. Fisher, E. Fowler, A. A. Fowler and R. Natarajan, *Antioxidants*, 2017, **6**, 55.
107 V. L. Tzounakas, A. T. Anastasiadi, V. Z. Arvaniti, V. Lelli, G. Fanelli, E. C. Paronis, A. C. Apostolidou, E. G. Balafas, N. G. Kostomitsopoulos, E. G. Papageorgiou, I. S. Papassideri, K. Stamoulis, A. G. Kriebardis, S. Rinalducci and M. H. Antonelou, *Redox Biol.*, 2022, **57**, 102477.
108 J. S. Raval, J. Fontes, U. Banerjee, M. H. Yazer, E. Mank and A. F. Palmer, *Transfus. Med.*, 2013, **23**, 87–93.
109 D. P. Facchi, A. C. Lima, J. H. de Oliveira, D. Lazarin-Bidóia, C. V. Nakamura, E. A. Canesin, E. G. Bonafé, J. P. Monteiro, J. V. Visentainer, E. C. Muniz and A. F. Martins, *Int. J. Biol. Macromol.*, 2017, **103**, 129–138.
110 S. P. Facchi, A. C. de Oliveira, E. O. T. Bezerra, J. Vlcek, M. Hedayati, M. M. Reynolds, M. J. Kipper and A. F. Martins, *Eur. Polym. J.*, 2020, **130**, 109677.